FE8 type laboratory testing of White Etching Crack (WEC) bearing failure mode in 100Cr6

Danielsen HK*[a], Gutiérrez Guzmán F[b], Muskulus M[c], Rasmussen BH[a], Shirani M[a], Cornel D[b], Sauvage P[b], Wu J[d], Petrov R[d,e], Jacobs G[b]

a: Technical University of Denmark, Department of Wind Energy, Frederiksborgvej 399, 4000 Roskilde, Denmark
b: RWTH Aachen University, Institute for Machine Elements and Systems Engineering (MSE), Schinkelstrasse 10, 52062 Aachen, Germany
c: Norwegian University of Science and Technology, Department of Civil and Environmental Engineering, NO-7491 Trondheim, Norway
d: Delft University of Technology, Department of Materials Science and Engineering, Mekelweg 2, 2628 CD Delft, Netherlands
e: Ghent University, Department of Electrical Energy, Metals, Mechanical constructions & Systems, Technologiepark 903 Zwijnaarde, 9052 Ghent, Belgium
***:** Corresponding author

Abstract

WEC is an aggressive and unpredictable failure mode affecting bearings in particular in the wind energy sector. This paper focuses on the most common used method for WEC laboratory accelerated testing, the FE8 type test rigs using martensitic through hardened 100Cr6 cylindrical roller thrust bearings, analyzing the load conditions, test results and damage quantification. The surface and sub-surface stress conditions as well as the surface frictional loading were analyzed using a half-space model. Simulations and experiments were conducted under different load conditions, including tests with different number of rollers and tests using dynamic load and speed. Tests under constant loads show a low load influence and prove that a WEC failure can occur both prematurely and after exceeding the rated lifetime. Dynamic conditions did not accelerate WEC failure, and only rollers (not washers) were affected by WEC under dynamic loading conditions. Damage characterization was performed using optical microscopy and ultrasound scanning. Advanced image analysis based on characterization of defect regions in the ultrasound scans was used for quantifying the subsurface damage. Tests showed WEC failure could be achieved consistently, however there were seemingly large random variations in the observed damage.

Introduction

A common cause for maintenance and downtime in the wind energy industry are premature bearing failures due to the so-called White Etching Cracks (WEC) [1-2]. This aggressive and unpredictable failure mode can be regarded as one of the most critical failure modes for wind turbine components [3-4]. It is characterized by subsurface crack networks within regions of altered microstructure that appear white in optical microscopy, called White Etching Areas (WEA) [5-6], and lead to axial cracking or spallation in the raceway. This widespread failure mode affects primarily gearbox bearings in wind turbines, but also affects the main bearings. Although the true extent of WEC failures cannot be quantified, WEC has for the last 20 years been responsible for a large number of system failures. While WEC has been studied intensively over the course of the last years, commercial satisfactory preventive

measurements are not available nor are there any predictive calculation methods. Although WEC is a common challenge in multiple fields of mechanical driveline technology, it has been proposed that the special transient load conditions [7-8] that wind turbines are subjected to, make this failure mode more prevalent in the wind energy sector compared to other sectors.

Several studies have been launched to understand and alleviate WEC formation in order to improve the reliability of wind turbine bearings. These include several different aspects such as heat and surface treatment solutions [9-11], reduced friction coefficient using Black Oxide coatings [12-14] and the influence of the oil and its additives on WEC formation [15-17]. In order to evaluate the influence of this variety of parameters on WEC formation, large testing campaigns should be performed. In order to conduct such studies in a reasonable time frame, reliable and rapid accelerated laboratory testing methods and conditions to reproduce WEC are required. Replicating WEC using laboratory scale bearing test rigs under pure mechanical load have only been successful in a few setups without resorting to highly aggressive conditions such as hydrogen pre-charging [18-19] or stray currents [20-21]. Currently the most established method of reproducing WEC under pure mechanical load is by using cylindrical roller thrust bearings (axial bearings) under constant loading conditions with FE8 type test rigs [22-29] originally intended to be used for testing lubricants standardized in DIN 51819-1:2016-12 [30]. By using lubricants with a chemical composition which promotes WEC formation, this test setup using constant load is a reliable way of forming WEC. However, this does not reflect the wind turbine environment where the bearings are subjected to transient loads [7-8]. In order to examine the impact of corrective measures for WEC with a high level of cost- and time effectiveness, more realistic accelerated WEC-tests at laboratory scale are needed that simulate wind turbine conditions. Furthermore, a method for quantifying the formation of WEC is needed in order to assess the influence of WEC drivers and preventive measures.

This paper takes a closer look at the FE8 type test rigs most commonly used for accelerated WEC tests and analyzes the effect of loads, investigates how dynamic load and speed affect the WEC formation, and quantifies the damage using ultrasound scans.

Experimental

Test set-up

The tests presented in this work were conducted using cylindrical roller thrust bearings of type 81212 in three laboratory FE8 type test rigs [31], see figure 1. Deviating from the standard FE8 constant load spring system, two of the test rigs (TR1 and TR2) were upgraded with a hydraulic load system which is capable of loads up to 100 kN, with load and speed cycles with up to 50 kN/s and up to 500 rpm/s settable in a load spectrum by a program. They include electrical servo-drives with steplessly adjustable speeds including shifted 2-speed gearbox for 7.5-4,500 rpm with automatic test-stop in case of exceeding temperature, vibration or runtime limit. Another test rig (TR3) with the standard statically loaded plate spring package, was used for conducting constant load tests. All test rigs are equipped with accelerometers to detect vibrations caused by bearing damages. The bearing positions have been named as B1 at the drive side and B2 at the axial load excitation side, A for the axle mounted washer and H for the housing mounted washer.

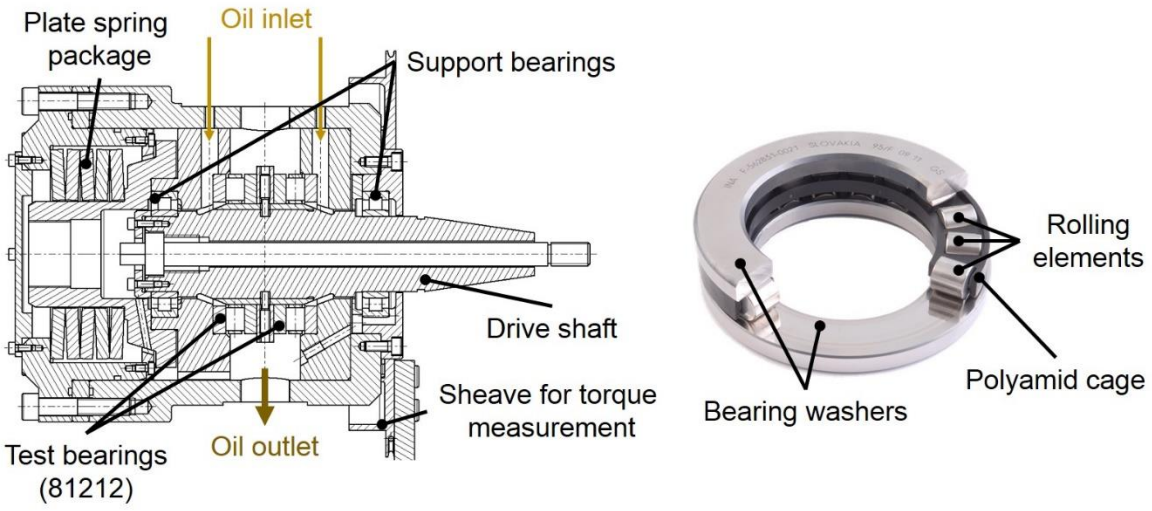

Figure 1: *FE8 type test rig with test bearings of type 81212 according to [31]. The bearing inner bore is 60 mm and roller diamater is 11 mm*

In all tests rolling elements and washers made from martensitic through hardened 100Cr6 steel (AISI 52100) from two different manufacturers were used. In order to avoid chemical influence, a polyamide cage (PA 66) was used instead of the usual brass cage. The test bearings used in TR1 & TR2 have 19 rolling elements from manufacturer 1, with a basic dynamic load according to the manufacturer of 137 kN. The arithmetic surface roughness R_a was measured to be on average 80 nm for the washers and 60 nm for the rollers. For TR3, bearings with both 19 and 15 rolling elements have been used from manufacturer 2, with a basic dynamic load according to the manufacturer of 172 kN in the case of 19 rolling elements. The basic dynamic load of the bearings with 15 rolling elements was calculated to be 144 kN according to DIN ISO 281 [32]. The arithmetic mean surface roughness R_a was measured to be on average 50 nm for the washers and 65 nm for the rolling elements.

Test conditions

All tests were run using a mineral oil in a circulating lubrication system with filters. This specific oil is a commercially available, fully formulated gearbox oil with a measured kinematic viscosity of 103.7 mm²/s at 40 °C and a viscosity index of 100. An analysis of the elemental composition is shown in table 1. Noteworthy is the presence of Ca-Sulfonate and Mg-Sulfonate, additives which are considered to promote a WEC induced failure [16].

Lubricant	S	P	Zn	Ca	Mg
ISO VG 100 mineral oil	8343 ppm	512 ppm	616 ppm	39 ppm	1950 ppm

Table 1: *Chemical analysis of the used mineral oil (VG100) - Measured by ICP*

In alignment with previously conducted investigations [26] the temperature of the housing mounted washer was controlled to be 100 °C. The shaft speed was kept constant through the test at 300 rpm, except during dynamic tests (Table 2). The evaluation of the lubrication conditions was carried out by calculating the specific lubrication film thickness λ_{min}, defined in equation 1. The isotherm lubrication film thickness h_{min} was calculated according to [33].

Equation 1:
$$\lambda_{min} = \frac{h_{min}}{\sqrt{\left(R_{a,Washer}^2 + R_{a,Roller}^2\right)}}$$

Tests under a constant load of 60 kN were carried out at all test rigs (TR1, TR2 & TR3), while tests under a constant load of 80 kN were conducted only in TR3. Tests using dynamic load and speed were conducted in TR1 & TR2. In all test rigs sudden-death testing was conducted until a specific vibration

threshold was surpassed, which was around 50 % - 100 % higher than the steady state vibration after run-in. Steady state vibration varied slightly for each test, however when the vibration level started to increase due to spallation it did so exponentially, passing the vibration threshold within a few hours. Analyzing sudden-death testing date allows a fairly accurate representation of the statistical behavior in a fraction of the test time that would have been necessary to test all units [25]. If no failure occurred tests were manually stopped after a pre-defined time.

Parameter set	**1**	**2**	**3**	**4**
Number of rolling elements	19	19	15	15
Axial bearing load [kN]	60	100	60	80
Shaft speed [min^{-1}]	300			
Bearing mass temperature [°C]	100			
Oil volume flow [l/min]	0.25			

Table 2: *Parameter sets for all conducted tests using cylindrical roller thrust bearings from type 81212 with 15 and 19 rolling elements (maximum load for dynamic tests)*

Due to the different load levels and different number of rolling elements, each individual parameter set listed in table 2 leads to different normal contact and subsurface stresses in the roller-washer contact.
In this work, the normal contact stress was calculated using both an active set strategy coupled with a conjugate gradient method and a semi-analytical method based on the half-space theory described in [34]. Therefore, typical limitations of the half-space theory applies here:

- The material of the contacting bodies is elastic and isotropic
- The contact zone is small in regard of the dimension of both bodies in contact

While smooth surfaces were adopted for the washers, a measured roller profile in roller axis direction was used. Material properties of both contacting bodies were assumed as similar with a young modulus of 210 GPa and a Poisson ratio of 0.3.

The shear stresses distribution in rolling direction and contact width direction are computed with a numerical algorithm described in [35] and the subsurface stress was computed using the semi-analytical approach described in [36]. The used calculation models had been previously validated with study cases given in the related literature. The coordinate system used for the simulations is presented in figure 2. Hereby describes *x* the rolling direction, *y* the contact width direction and *z* the depth.

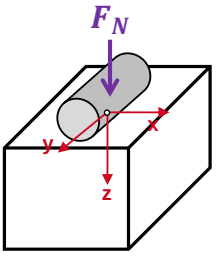

Figure 2: *Coordinate system for the contact stress and subsurface stress simulations of the roller-washer contact from cylindrical roller thrust bearings of type 81212*

In this work it is assumed that all roller-washer contacts experience an equivalent load and, therefore, equivalent sub-surface stresses. In reality, however, each contact can experience minimal variating loads. This can result on the one hand from local differences such as roller profile deviations. On the other hand different bearing fittings can lead to slightly different hoop stresses between washers, which in turn result in different sub-surface stresses for the axle mounted washer (A) and for the housing mounted washer (H). Experience has also shown that in air cooled FE8 type test rigs, such as

the ones used in this work, the drive side bearing (B1) experiences a higher temperature that the bearing on the axial load excitation side (B2). For the conditions used in this work usually 2 °C – 5 °C higher.

Ultrasound

For ultrasonic scans a Pulse-Echo technique was used with a high frequency HFUS 2000 system with a X, Y, Z scanner immersion scanning system in a 1000 x 700 x 500 mm water tank. During scanning, the peak echo values are measured in two electronic time gates. The first gate is covering the cross section of the bearing and the second gate is covering the back echo from the inner surface of the bearing. Frequency of the transducer is set to 50 MHz and moves in the x- and y-coordinates with a resolution of 0.200 mm (-6 dB limit) per measurement in both directions, which is the estimated size of WEC that should be readily detectable. Scanned objects were cleaned for lubrication oil to avoid aberrations in the scan and dried afterwards to avoid corrosion from the water, which acts as medium between the examined object and the detector. All washers from tests conducted in TR1 & TR2 were scanned for subsurface cracks, only in some cases were rollers scanned.

Microscopy

The cross-section of selected samples were extracted from the raceways and rollers by a Struers® Secotom-10 cutting machine, with a feeding speed of 0.03 mm/s to avoid significant heat and the consequent microstructure changes. The cross-section samples were mechanically ground using Struers paper # 320 - # 2000. Subsequent polishing until 1 µm suspension was done before etching with 2 vol% Nital (solution of 2vol% nitric acid in ethanol) for 15 s at 20°C.

Results

Surface and sub-surface stress calculations

The contacting bodies are assimilated to half-spaces, and their contact surfaces meshed into a 500 x 500 x 100 (x; y; z) elements grid, with each cuboidal element having a dimension of 0.38 µm x 13 µm x 1.9 µm. The resulting maximum normal contact stress for each parameter set is shown in Table 3. Figure 3 shows exemplary the normal contact stress distribution for parameter set 4 in table 2.

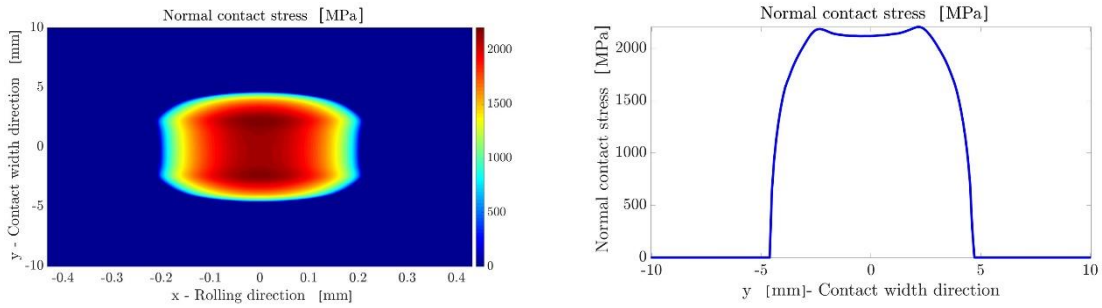

Figure 3: *Exemplary presentation of the calculated normal contact stress distribution in the roller-washer contact of a cylindrical roller thrust bearing from type 81212 with 15 rolling elements under a constant axial load of 80 kN (parameter set 4 according to table 2)*

As a result of the normal contact stresses and the bearing kinematics, the surface of thrust bearings is exposed to a high frictional loading, which can be quantified by the product of the spatially resolved pressure and the sliding velocity ($p \cdot v_{sliding}$). The resulting maximum values for the energetic criteria and their position along the contact line are shown also in table 3 for all parameter sets. For the purpose of illustration the $p \cdot v_{sliding}$ is plotted in figure 4 along the contact line of the roller-washer contact in width direction (*y* axis according to figure2).

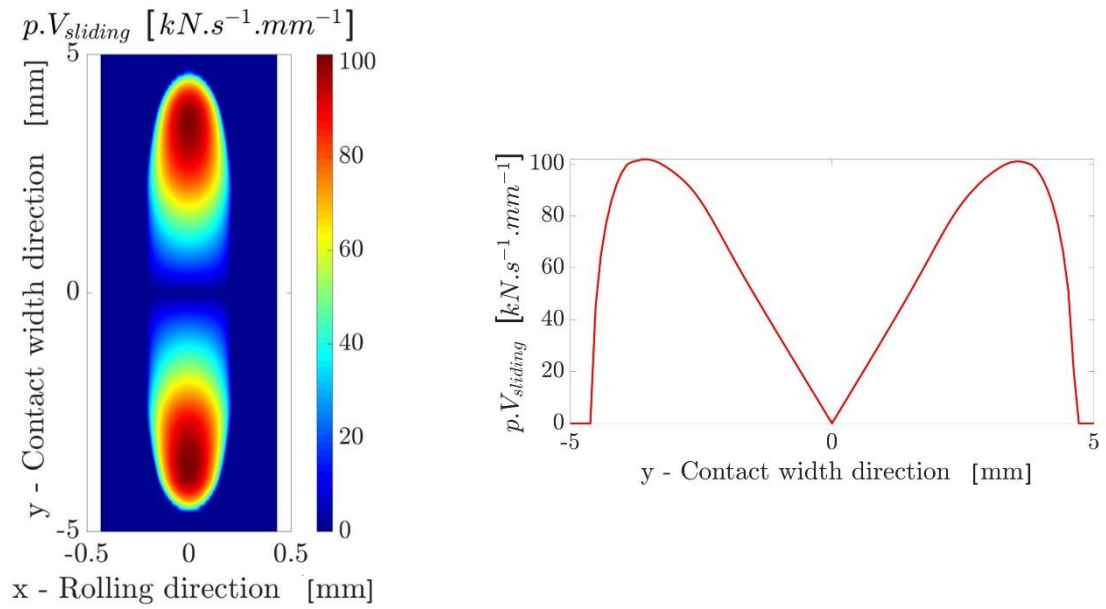

Figure 4: *$p \cdot v_{sliding}$ along the roller-washer contact line of a cylindrical roller thrust bearing from type 81212 with 15 rolling elements under a constant axial load of 80 kN at a constant shaft speed of 300 min^{-1} under consideration of the normal contact stress distribution shown in figure 3 (parameter set 4 according to table 2)*

Parameter set	1	2	3	4
Contact pressure [N/mm²]	1,788	2,191	1,965	2,202
$p \cdot v_{sliding,Max}$ [kN/(s·mm)]	75	102	86	102
Position $p \cdot v_{sliding,Max}$ [mm]	± 3.2	± 3.4	± 3.4	± 3.5
λ_{min}	0.38	0.45	0.47	0.45

Table 3: *Contact and lubricating conditions in the cylindrical roller thrust bearings from type 81212 for parameter sets given in table 2*

It is worth adding that as a result of the bearing kinematics, the motion of a roller is composed by a rolling motion around the roller axis and a spinning motion around the normal to the contact surface. The rolling and the spinning motions result in a tangential force and a spinning moment implied in the contact surface in order to restore the rolling equilibrium [37]. Although tangential load, spinning moment and normal load occur at the same time, two simplified separate simulation cases are implemented in this work for determining the sub-surface Tresca stresses. As shown in figure 5 the normal load is combined either with a pure spinning moment or with a tangential force on the roller.

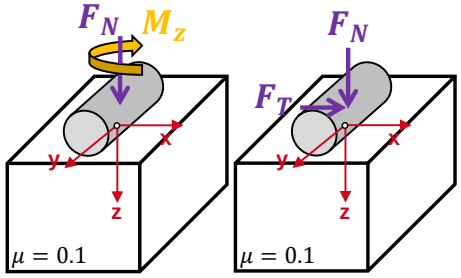

Figure 5: *Considered simulation cases: a) rolling motion around the roller axis and spinning moment around z-axis b) rolling motion around the roller axis and tangential force implied in the roller-washer contact surface*

Considering the spinning moment (simulation case 1, figure 5), the resulting shear contact stresses are distributed tangentially around the contact surface center. The projection of these tangential contact shear stresses on the rolling direction axis (*x*-axis) and on the contact width direction axis (*y*-axis) are represented on figure 6a and 6b for parameter set 4 according to table 2.

As shown in figure 6a the shear contact stress in rolling direction is antisymmetric to the *xz*-plane at *y* = 0 mm. On the other hand and as shown on figure 6b the shear contact stress in width direction is antisymmetric to the *yz*-plane at x = 0 mm. Due to the distribution of the shear contact stress the subsurface Tresca stress distribution is also antisymmetric to both the *xz*-plane (*y* = 0 mm) and the *yz*-plane (*x* = 0 mm). The distribution of Tresca stress for parameter set 4 (Table 2) is shown in figure 6c at three different planes: maximum $p{\cdot}v_{sliding}$ plane (*y* = ± 3.55 mm), maximum Tresca stress plane (*y* = ± 2.2 mm) and the *xz*-plane (*y* = 0 mm). While the Tresca stress under the position of maximum $p{\cdot}v_{sliding}$ reaches a maximum of 1,116 MPa at a depth *z* = 0.13 mm, the absolute Tresca stress maximum of 1,377 MPa is localized at the depth *z* = 0.15 mm (see Table 4).
As also shown in figure 6c the domain of negative slip (negative *y*-values) is characterized by a negative shear stress in rolling direction and a displacement of the relative subsurface shear stress against rolling direction. The opposite observation can be done for the domain of positive slip (positive *y*-values).

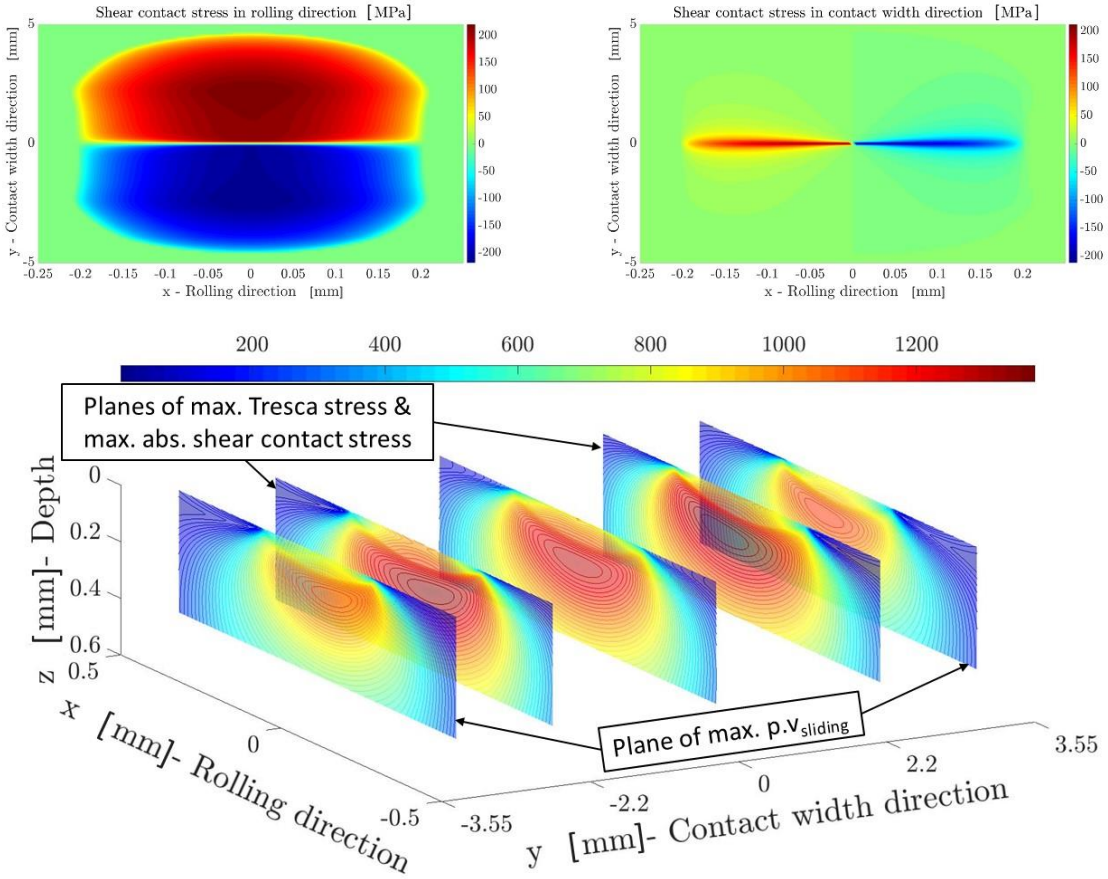

Figure 6: *Exemplary presentation of the calculated: (a) shear contact stress in rolling direction, (b) in contact width direction and (c) Tresca stresses at the maximum plane (y = ± 2.2 mm), the xz-plane (y = 0 mm) and the plane of maximum $p{\cdot}v_{sliding}$ (y = ± 3.55 mm) in the roller-washer contact of cylindrical roller thrust bearing from type 81212 with 15 rolling elements under a constant axial load of 80 kN (parameter set 4 according to table 2). Calculation is carried out under consideration of the rolling motion around the roller axis and spinning moment around z-axis (simulation case 1 according to figure 5)*

If in contrast instead of the spinning moment (simulation case 1, figure 5) only the tangential force (simulation case 2, figure 5) is considered, the shear contact stress is symmetrical to the *xz*-plane at *y* = 0 mm (figure 7a). Consequently, the subsurface Tresca stress distribution is equally distributed in both planes of maximum $p{\cdot}v_{sliding}$ (y = ± 3.55 mm) as shown in figure 7b. The maximum Tresca stresses

under these positions are localized at the depth z = 0.13 mm with the magnitude 1,116 MPa and is consistent with the previous results from simulation case 1 (figure 5).

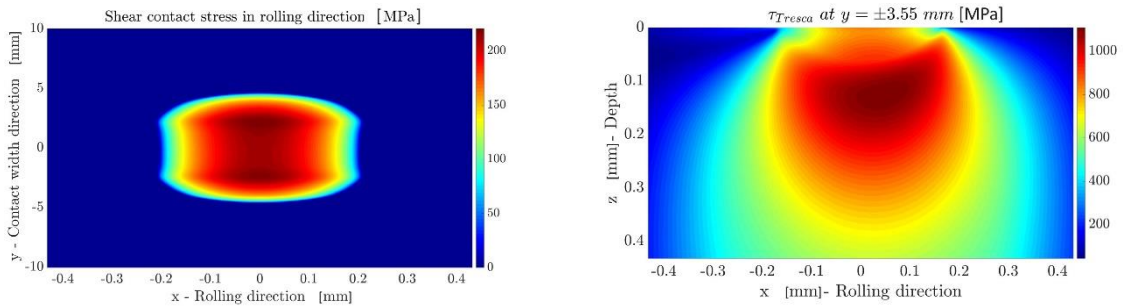

Figure 7: *Exemplary presentation of the calculated: (a) Shear contact stress in rolling direction and (b) Tresca stress at the position of maximum $p \cdot v_{sliding}$ (y = ± 3.55 mm) in the roller-washer contact of cylindrical roller thrust bearing from type 81212 with 15 rolling elements under a constant axial load of 80 kN (parameter set 4 according to table 2). Calculation is carried out under consideration of the rolling motion around the roller axis and tangential force implied in the roller-washer contact surface (simulation case 2 according to figure 5)*

It can be, therefore, concluded that the maximum Tresca stress values and their depths are similar in both simulation cases. However, by considering the spinning moment the distribution of the Tresca stress distribution is antisymmetric to the *xz*-plane at *y* = 0 mm and the *yz*-plane at *x* = 0 mm, reflecting the effect of negative and positive slip. By considering the tangential force instead the Tresca stress distribution is on the other hand symmetrical to the *xz*-plane at *y* = 0 mm but unsymmetrical to the *yz*-plane at *x* = 0 mm. The maximal Tresca stress is, however, for both cases located at similar *y*- and *x*-planes as shown in figure 8.
Furthermore, the simulation show that the maximum Tresca stresses and the maximum energy input (expressed by $p \cdot v_{sliding}$) reach their maximum at different raceway diameters (*y*-axis). The computed maximum Tresca stresses and their positions in *y*- and *z*-direction for both simulation cases and all load cases are summarized in the table 4.

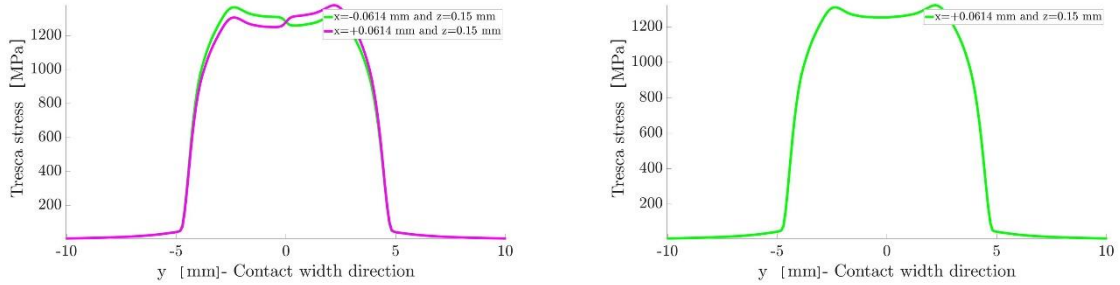

Figure 8: *Exemplary presentation of the calculated maximum Tresca stress under consideration of: (a) the rolling motion around the roller axis and spinning moment around z-axis (simulation case 1 according to figure 5) and (b) the rolling motion around the roller axis and tangential force implied in the roller-washer contact surface (simulation case 2 according to figure 5)*

Parameter set	1	2	3	4
Max. Tresca stress [MPa]	1,116	1,370	1,227	1,377
Depth of max. Tresca stress [mm]	0.125	0.154	0.137	0.155
Y-Position of max. Tresca stress [mm]	± 2.152	± 2.2	± 2.167	± 2.2

Table 4: *Calculated magnitude and depth of the maximum Tresca stress in the roller-washer contact of cylindrical roller thrust bearings from type 81212 for all parameter sets according to table 2 and for both simulation cases using a constant coefficient of friction (μ=0.1)*

Test results and characterization

10 tests were run on TR1 & TR2 to produce WEC and investigate the influence of the dynamic loads [7-8] on WEC formation, see table 5. After dismounting, visual inspection was done for all washers and rollers. Test 1 through 4 ran at a constant load of 60 kN under same conditions to gather statistical data for analysis of WEC formation, all bearings failed within the time span of 100-170 h. For test 1, 2 and 4 spallation was observed on both washers and rollers while in test 3 there was only damage on the washer. Tests 5 and 6 ran with a dynamic load with 0-100 kN in a 10 s cycle to simulate load fluctuations. Test 5 was interrupted at 200 h, however spallation was observed on one of the rollers, while test 6 failed at 198 h with spallation on several rollers. The washers were not affected by spallation although there was follow-up damage in the form of indentations from spalled off metal particles from the rollers. For simulating simultaneous load and speed changes tests 7 through 9 were run with both dynamic 0-100 kN load and 0-300 rpm speed cycles. Test 7 ran with load and speed in-phase with 10 s cycles, test 8 with in-phase 4 s cycles and test 9 with out-of-phase 4 s cycles. None of the in- or out-of-phase tests showed any damage on either rollers or washers. Test 10 was run with constant load and dynamic 0-300 rpm speed in 4 s cycles and was the only dynamic test that showed damage on the washers, but there was no damage on the rollers.

Test number	Speed [rpm]	Load [kN]	Cycle [s]	In/out of phase	Test time [h]	End criteria	Washer damage	Roller damage
1	300	60	-	-	141	Vibration	Yes	Yes
2	300	60	-	-	170	Vibration	Yes	Yes
3	300	60	-	-	100	Vibration	Yes	No
4	300	60	-	-	144	Vibration	Yes	Yes
5	300	0-100	10	-	200	Time	No	Yes
6	300	0-100	10	-	198	Vibration	No	Yes
7	0-300	0-100	10	In	606	Time	No	No
8	0-300	0-100	4	In	173	Time	No	No
9	0-300	0-100	4	Out	282	Time	No	No
10	0-300	60	4	-	300	Vibration	Yes	No

Table 5: *Test conditions and results from the accelerated WEC tests in TR1 & TR2*

All washers were scanned using ultrasound, which showed different stages of subsurface crack formation in all washers from tests 1 through 4 and test 10, no subsurface cracks were found in the washers from tests 5 through 9. Figure 9 shows the difference between a damaged washer from test 2 and an unaffected washer from test 6. The large blue features in figure 9 left indicate lack of back-echo due to spallation while the smaller green or dark yellow features are suspected to be subsurface cracks. The notches at the 12 clock positions of the washers were used for orientation when extracting specimens for microscopy. Scans of rollers from test 5 and 6 showed a clear band of subsurface cracks all along the entire circumference, shown in blue in figure 10. In general, it was observed that the damage in the washers has occurred mostly in the outer band of the raceway (positive slip), while for the rollers the damage was correspondingly in the outer part of the roller (negative slip). Analyzing the ultrasound scan of the washers the subsurface damage was located 1.5 mm to 4.5 mm from the centerline, which is in correspondence with the calculated position of $p \cdot v_{sliding,Max}$ being 3.2 mm and the maximum shear stress being 2,1 mm, see table 3 and 4.

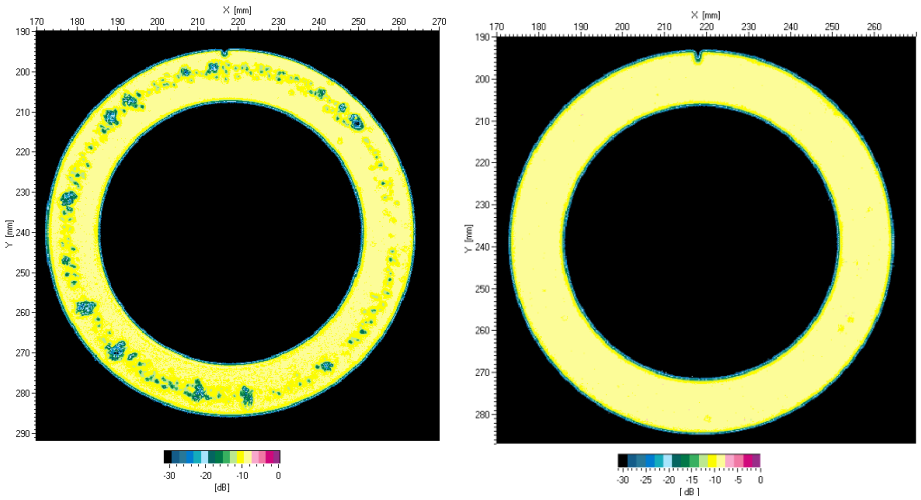

Figure 9: *Ultrasonic scans from (a) washer B2H from test 2 showing spallation in blue and subsurface WEC in green, and (b) washer B2H from test 6 showing no subsurface damage.*

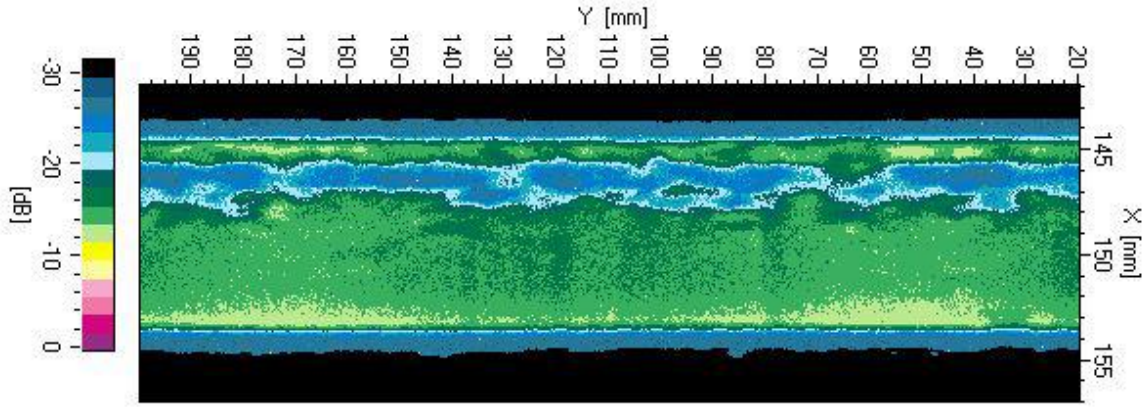

Figure 10: *Ultrasound scan in a roller from test 6 showing a band of WEC (blue) within the undamaged steel (green). The top and bottom blue color indicate the chamfering of the roller.*

Cross-section samples for metallurgical investigations were extracted from both raceways and rollers, which then were analyzed using optical microscopy to confirm the presence of WEC. Specimens from all of the washers were extracted from sites where subsurface defects had been identified by ultrasound, as shown in figure 11, as well as from sample rollers, see figure 12. Extensive WEC damage at sites chosen using the ultrasonic scanning technique confirmed this to be an effective method to detect and locate subsurface cracks in both washers and rollers. The metallographic observations of more than hundred cracks showed a close correlation between the subsurface cracks and WEA, identifying almost all (>90%) of the subsurface cracks as being of the WEC type. The formation of WEC was generally found to be at a depth of 100-150 µm, corresponding well with the calculated Tresca stress 125 µm in table 4, but some cracks were located deeper as well. It was observed that a few of the cracks had propagated to the surface, where they would cause spallation given enough time, which in turn causes the vibration level to increase sharply and stop the test.

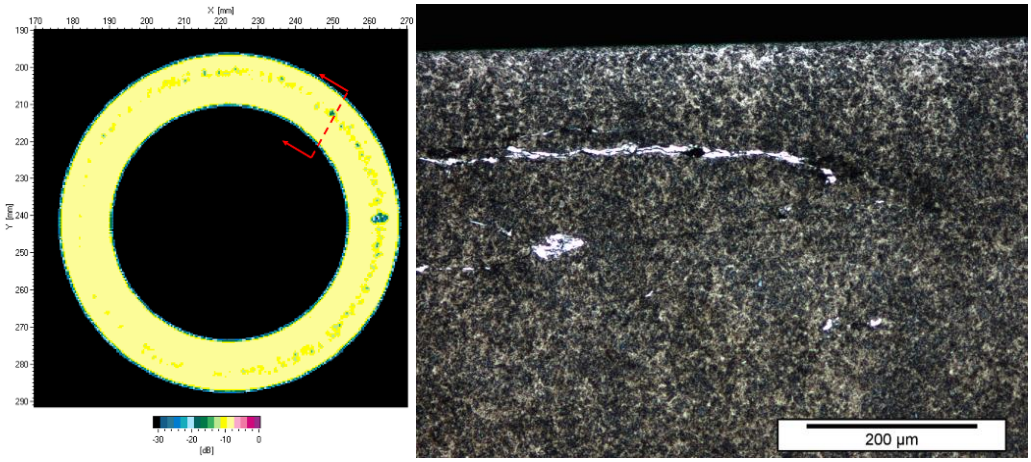

Figure 11: (*a) Ultrasound scan from test 4 washer B1A, showing in red the cut where figure 11b was taken. (b) Optical microscopy image of a WEC with a visible white etching area around the crack.*

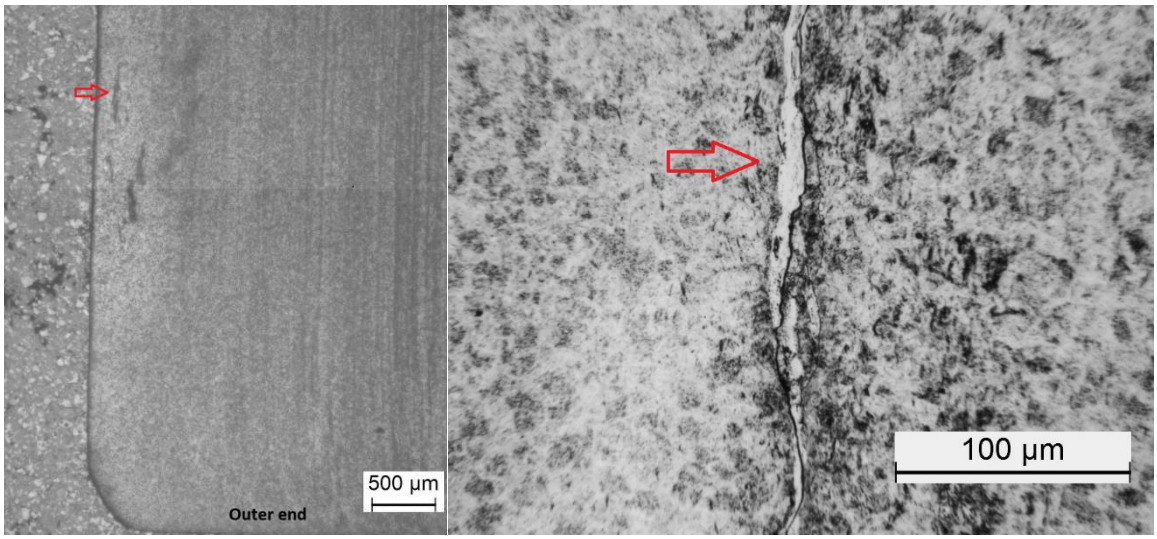

Figure 12: *Optical microscopy of a roller from test 6 cut along the longitudinal axis. Same WEC is observed in (a) and (b) indicated by red arrow at different magnifications.*

For the purpose of comparability and statistics, other tests conducted in TR3 (using bearings from another manufacturer) are presented in table 6. Tests 11 through 13 were conducted under same conditions as used in tests 1 through 4, while tests 14 through 17 show the effect of reducing the number of rollers and tests 18 through 25 the effect of increasing the load. All tests stopped due to vibration except for test 17 which did not fail and was manually stopped after 400h. The failure was usually caused by the bearing washers, therefore the roller damages are more likely to be consequential. A closer look at the failed bearing components reveals, that 57.1 % of the initial failures could be traced back to the shaft washers. In contrast, 14.3 % of the failures were traced back to the housing washers and 28.6 % to the rolling elements. The highest failure rate of the shaft washers (64 %) occurred in the tests conducted with an axial load of 80 kN (parameter set 4, table 2). Although the different reliability of the bearing components is not ensured statistically, the observed tendency could be related to temperature deviations between the washers, which in turn are influenced by the lubricant temperature. In the used test rigs the oil is fed directly on the housing washer so that the shaft washer is cooled subsequently resulting in a higher washer temperature. An influence of the temperature on the damage occurrence at otherwise comparable contact conditions was also shown in [38]. Associated microstructural analysis of selected specimens can be found in [39] and 3D characterization of crack network in [40]. As a result of these investigations, it can be noted that the tests failed due to WEC regardless of the applied load and number of rolling elements. In addition

more detailed investigations in [25,39] reveal, that the starting point of the WEC damage is below the surface and lies in the area of negative slip of the washer which correlates roughly with the aforementioned positions of maximum $p \cdot v_{sliding}$ and the maximum shear stress.

Test number	Load [kN]	Rollers	Test time [h]	End criteria	Washer damage	Roller damage
11	60	19	222	Vibration	Yes	No
12	60	19	270	Vibration	Yes	Yes
13	60	19	395	Vibration	Yes	No
14	60	15	275	Vibration	Yes	Yes
15	60	15	296	Vibration	Yes	Yes
16	60	15	199	Vibration	Yes	No
17	60	15	400	Time	No	No
18	80	15	50	Vibration	Yes	Yes
19	80	15	70	Vibration	Yes	No
20	80	15	89	Vibration	Yes	No
21	80	15	90	Vibration	Yes	No
22	80	15	120	Vibration	Yes	Yes
23	80	15	127	Vibration	Yes	No
24	80	15	130	Vibration	Yes	No
25	80	15	148	Vibration	Yes	No

Table 6: *Test conditions and results from the accelerated WEC tests in TR3 at 300rpm.*

Discussion

Time to analysis failure

The evaluation of rolling bearing tests regarding the service life is commonly carried out using the Weibull analysis [41]. Representative for the results of a Weibull analysis is the Weibull line, which is drawn in a double logarithmic diagram based on the individual failures or run-throughs. The Weibull line is therefore the graphical representation of probability of failure or survival for a specific run time. The Weibull line itself is characterized by the shape parameter beta (β) and the characteristic lifetime η (lifetime at a failure probability of 63.2 %). With a higher shape parameter indicating a smaller dispersion of the test results. Typical values for the shape parameter for roller bearings are in the range of 1 to 2 [42-44] for subsurface initiated fatigue, which is controlled by the randomly distributed material defects. In contrast, surface initiated fatigue leads to shape parameters around 2 and corrosion leads to values in the range of 2 to 3.5 [45]. Regarding WEC induced failures, the recent literature describes that the associated beta value is larger than 1, such as 2.5 to 3.5 in [46], 3 to 4 or higher in [47] and 3 to 10 or higher in [48]. The typical Weibull diagram is shown in the figure 13 for the tests conducted in TR3 using parameter set 4 according to table 2.

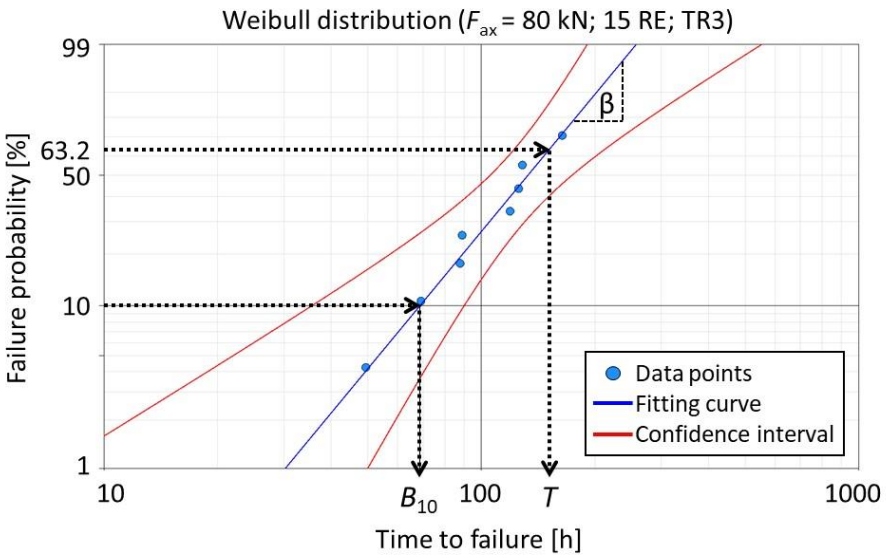

Figure 13: *Weibull diagram for the tests conducted using parameter set 4 (cylindrical thrust roller bearings with 15 rolling elements under a constant load of 80 kN at a shaft speed of 300 rpm) including exemplary presentation of the Weibull shape parameter beta β, the characteristic lifetime T and the experimentally determined lifetime at a failure probability of 10 % B_{10}*

When comparing the given values with the literature, it must be taken into account that the Weibull parameters can be determined using different methods. Often the Median Rank Regression (MRR) or the Maximum Likelihood Estimation (MLE) are used [49], but in some of the aforementioned references it is not always specified which method was used. While the MRR is a procedure for estimating the Weibull parameters by fitting a least squares regression line through the points on a probability plot [49], the MLE is a classic numerical method for calculating parameters for large sample sizes [41]. Especially with small sample sizes (n < 10), the parameters can be overestimated using the MLE-Method, leading to too large beta values [41]. Due to its suitability for smaller samples, the MRR-Method is used in the following evaluation of the Weibull line. A detailed introduction to the MRR procedure can be found in the corresponding standard DIN EN 61649 [41]. In addition, the tests were carried out using the sudden death method, resulting in an adapted ranking calculation within the scope of the evaluation. Further information to the sudden method can also be found in [41].

The results of the Weibull analysis of the performed tests, the calculated rated life time of the bearings according and the modified rated life time according to DIN ISO 281 [32] are shown in table 7. A more detailed presentation of the parameters used for the modified life time calculations can be found in appendix A. The plotted Weibull results are shown in Figure 14.

Test rig	TR1 & TR2	TR3	TR3	TR3
Bearing axial load [kN]	60	60	60	80
Rolling elements	19	19	15	15
Test runs	4	3	4	8
Contact load [kN]	3.16	3.16	4.00	5.33
Contact pressure [N/mm²]	1,788	1,788	1,965	2,202
Shape parameter β	4.69	2.81	3.18	2.85
Characteristic lifetime η [h]	174.80	325.06	319.44	150.91
Experiment lifetime B_{10} [h]	108.15	146.24	157.54	68.68
Basic rating life L_{10} [h]	870.85	1859.09	1028.21	394.11
Modified rating life L_{10m} [h]	163.88	326.55	191.35	68.41
B_{10}/L_{10m}	0.66	0.45	0.82	1.00

Table 7: *Results of the Weibull analysis and comparison of the lifetime for tests run under constant load*

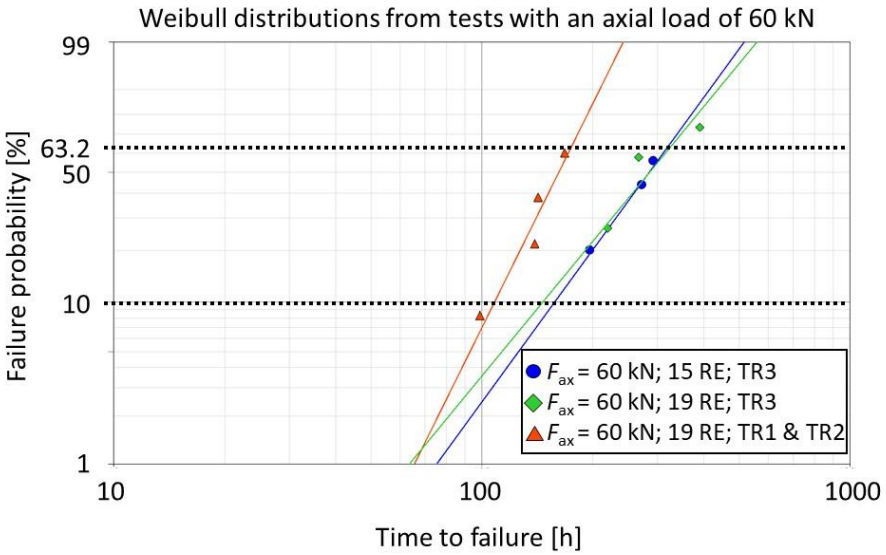

Figure 14: *Weibull diagram for the tests conducted under a constant load of 60 kN using cylindrical thrust roller bearings with 15 and 19 rolling elements (see table 2 for further test parameters)*

As shown in table 7 it can be noticed that the calculated beta values are in the aforementioned ranges for WEC induced failures. The B_{10} represents the lifetime at a failure probability of 10 % and is often determined during the evaluation within the Weibull analysis and represents, therefore, an experimentally determined value (see Figure 13). The B_{10} thus enables a direct comparison with the calculated L_{10m} according to DIN ISO 281 [32]. As expected, the tests conducted in TR3 show that by increasing the contact pressure, either by reducing the number of rollers or increasing the axial load, both the L_{10m} and the B_{10} decreases. Furthermore, it becomes evident that by decreasing the contact pressures the bearing failures occur sooner with regard of the modified rated life time. This behaviour can be pictured using the ratio between B_{10} and L_{10m}. For example, at a contact pressure of 2,202 N/mm² the bearing failures occur around the rated L_{10m} and cannot be considered as early failures. Nonetheless, it should be noted that it has been shown that using similar conditions and different lubricants the L_{10m} can be significant exceeded. In contrast, at a contact pressure of 1,965 N/mm² and 1,788 N/mm² the bearing failures occur at 82 % and 45 % of the rated L_{10m} respectively, thus can be considered as premature failures. These results demonstrate that the load influence is in this case lower than it should be according to the bearing fatigue theory. Furthermore, a WEC induced failure can occur both before and after the rated life time L_{10m}, thus not all WEC failures can be considered as premature failures.

A direct comparison of the tests from TR1, TR2 and TR3 run with a load of 60 kN and 19 rolling elements shows significant deviations for both the characteristic lifetime T and the B_{10} (Table 7). Under the assumption that the used test rigs perform identical, the occurred discrepancy can probably be attributed to the bearings being from two different manufacturers, with different dynamic load rating (difference of about 20 %) and therefore different load carrying capacity. Further noteworthy is the fact that the failure in tests from TR3 was concentrated in the inner band of the raceway (negative slip), correlating with the observations made in [15, 29, 50], whereas tests from TR1 & TR2 showed WEC mostly in the outer band of the raceway (positive slip). This is contradictory to the results seen in the tests from TR3 and the literature and cannot be explained at the moment.

Effects of dynamic loads

One of the main purposes of this work was to test the influence of dynamic loads on WEC failure using the FE8 type test rigs with axial bearings. While WEC could be provoked in all constant load tests for

TR1 & TR2 in a relatively short time, less than 170 h, all tests run under dynamic load or speed had longer time to failure, and for some cases there was no failure at all, even when tests lasted more than 600 h. Thus the dynamic loads/speed did not accelerate the time to failure, but rather delayed it. This could be related to the WEC failure mechanism in the FE8 type test rigs being dependent on the frictional loading ($p \cdot v_{sliding}$), where a constant load of 60 kN will have a higher accumulative energetic input than a dynamic 0-100 kN load. In it is also suggested in [29] that there is an influence of the time between subsequent contact load cycles (regeneration time), this would also further delay WEC formation when run under dynamic conditions. Using dynamic 0-300 rpm speed will only further reduce the energy input and increase regeneration time compared to a constant 300 rpm. It is curious though, that under dynamic load only the rollers failed with the washers showing no signs of damage at all, even with ultrasound scanning. In contrast, when using constant load, including dynamic speed, there was always damage on the washers. Thus the dynamic load only causes WEC in the rollers but not the washers, which is the opposite of what is observed for wind turbines, where it is typically the inner or outer rings that fail from WEC, but not the rollers.

Damage quantification

Test results from table 5 and 6 only give a time to failure parameter, but otherwise say nothing of the level of WEC formation in the bearings. Therefore, a method for quantifying the WEC formation in tests 1 through 4 has been investigated, consisting of an image analysis to quantify the subsurface damage in the bearings from ultrasound scans. From this analysis, a number of parameters are estimated that describe the status of the bearings. The data for analysis consists of the ultrasound images of the 4 tests with two bearings run in parallel, thus 20 washers in all. The analysis was performed using the Image Processing Toolbox in MATLAB (MathWorks Inc., Version R2016a). The original images show the ultrasound attenuation in a discrete color-coded scale with 16 different levels (figure 15a). The images were transformed into indexed images, with values from 1 to 16 for the attenuation parameter, ordered in descending magnitude, and 0 for the background. For example, an attenuation of -10 db was mapped to the index 6 and a stronger attenuation of -20 db was mapped to the index 11.

The region of interest (ROI) in the images was defined by selecting three ellipses (figure 15b). The first and second ellipses restrict the ROI to the annulus where the bearing surface was scanned. The third ellipse was occasionally used to exclude a small area in the top of the bearing that was due to a notch marker, see figure 9 (not visible and therefore not used in the example in figure 15).

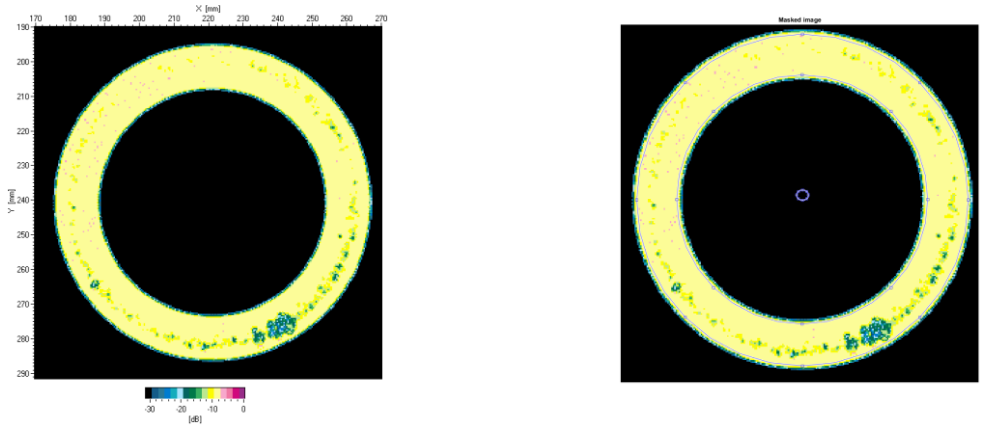

Figure 15: *Example of image preprocessing. A bearing with extensive damage is shown, from test 1 washer B2H. (a) Original image with axes and color-bar. (b) Definition of the image mask using ellipses.*

After extracting the ROI, a global threshold was applied. Each pixel in the ROI with a value > 6 (that is at least -12 db attenuation) was included in the further analysis. The attenuation values were shifted

by the same amount, so that -12 db then corresponded to a value of 1 and -20 db to a value of 5, for example. Figure 16a shows the resulting image data using the original color map.

In order to analyze the distribution of the damage across the bearing surface, two different methods were tested to determine the individual regions of interest. In the first method, the image was transformed to a binary mask [51] as implemented in the MATLAB function *imbinarize*. This adaptive thresholding method resulted in a further reduction of the area of interest (figure 16b). In the second method, the watershed transform [52] was used to split some of the binary regions into separate damage clusters (figure 16c). This method avoids a further thresholding operation and corresponds more acutely to the notion that cracks grow locally around initial subsurface defects. The subsequent analysis should be slightly more accurate using this advanced segmentation technique. Therefore in the following only the results for the watershed transform are further discussed.

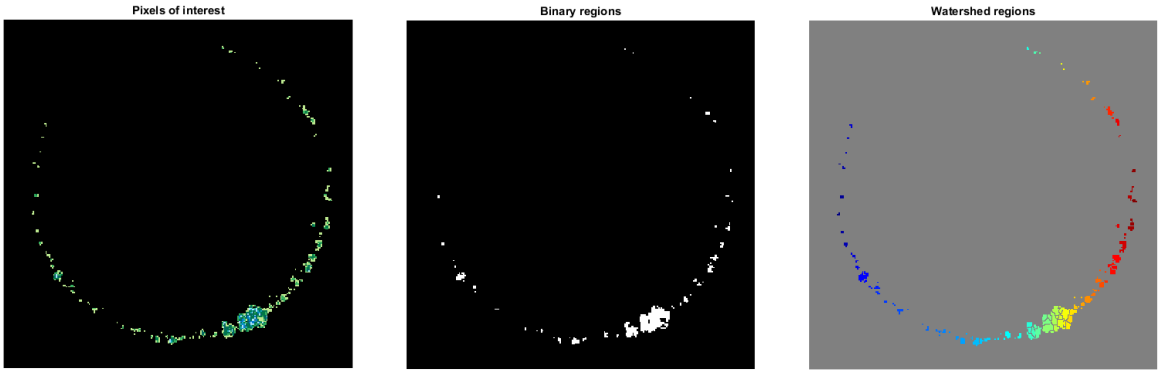

Figure 16: *Segmentation of damaged areas. Example using data from figure 15. (a) The pixels of interest after applying a global threshold. (b) Identified regions with subsurface damage. (c) More detailed clustering of damaged areas with the watershed transform. The colors indicate different defect regions*

The identified defect regions were subject to statistical analysis. The first parameter of interest is the amount of damage identified for each bearing. As the number of pixels in the original images varied somewhat, the defect area was normalized by the number of pixels in the region of interest. In most cases the affected area ratio shows significantly larger values for one of the two bearings per test and it was assumed that this corresponds to the bearing failure that stopped the test (due to vibrations detected above a constant threshold). In the 4^{th} test, both bearings showed similar defects and it seems that the test was stopped due to imminent failure(s) of either bearing. As these results are somewhat inconclusive (showing similar damage in both bearings, but less damage than for the cases where clearly one of the two bearings failed), the 4^{th} test was not considered in the subsequent analysis.

The distribution of area ratios for each bearing is shown in figure 17a. The curves are kernel density estimates of the probability density of a given area ratio in a failed (blue curve) or non-failed (orange curve) bearing. The individual area ratios are additionally indicated by the rugged lines at the bottom. As there is some overlap in the two distributions, the area ratios were in a second step averaged for both washers of each bearing. This led to much better discrimination of the two distributions (figure 17b).

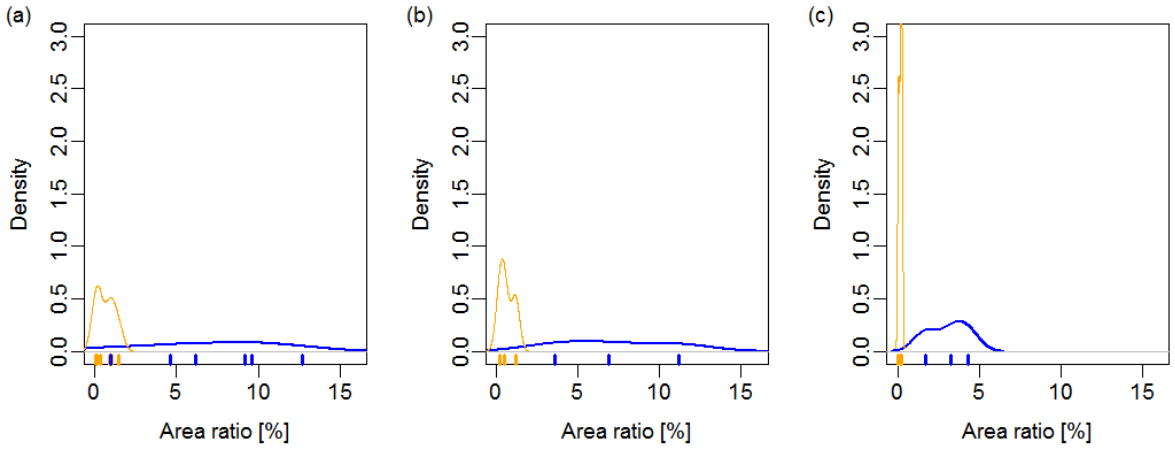

Figure 17: *Probability density function of defect area ratios from watershed segmentation, using kernel density estimation with automatic choice of bandwidth parameter. The rugged lines at the bottom indicate the individual area ratios on which these density estimates are based. (a) All available data points (n=12) with clearly identified damage (blue: failed bearing, orange: second bearing). (b) After averaging the two washers of each bearing (n=6). (c) Additionally using the more detailed information from the attenuation levels.*

The mean area of defect for the failed bearings was 7.20 ± 3.80 percent, compared to 0.64 ± 0.49 percent for the non-failed bearings (Figure 17b). In order to use the information contained in the different values of the attenuation parameter, the analysis was repeated by weighting the pixels with defects according to the discrete level of attenuation, thereby increasing the values of these area ratios for larger observed attenuation. The results further improved thereby (figure 17c). In this approach, the mean weighted defect area for the failed bearings was 3.10 ± 1.34 percent, compared to 0.17 ± 0.11 percent for the non-failed bearing.

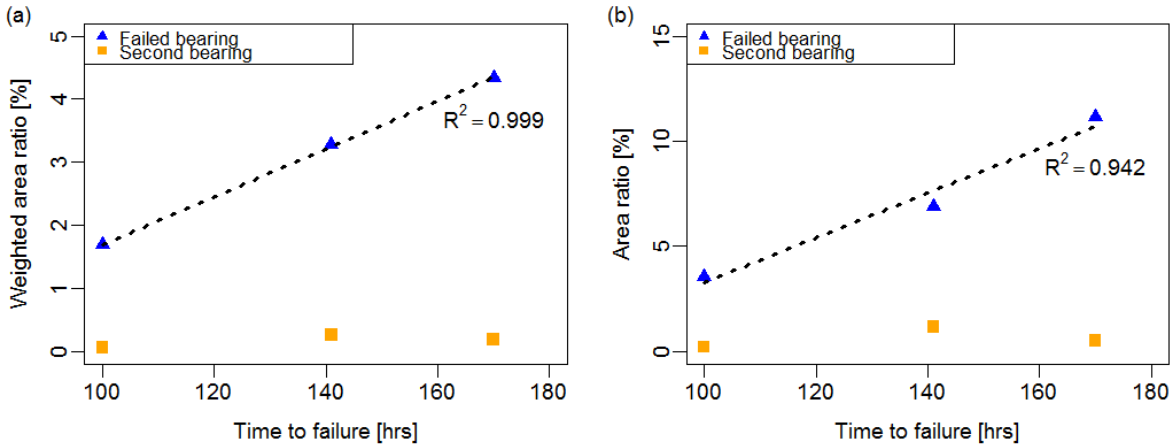

Figure 18: (a) *Correlation between failure time and image analysis results. (a) Weighted defect area ratio (averaged over the two sides of each bearing washer) versus failure time. Including all bearings with clearly identified failures (n=6). The dotted lines correspond to the least-squares regression fit. (b) For comparison purposes: Same as left panel, but for unweighted defect area ratios.*

Results indicate damage accumulates with time until sudden death occurs due to vibration from spallation. The weighted defect area correlates well with the time to failure (Figure 18a), the regression is almost perfect (R^2 = 0.999, p-value = 0.010). For unweighted defect areas (Figure 18b) the correlation is somewhat less distinctive (R^2 = 0.942, p-value = 0.108). This strong correlation between time to failure and area ratio suggests that image analysis, in particularly the weighted area ratio, is a promising tool to quantify bearing damage. As the current damage quantification is only based upon 3 tests, there is insufficient evidence to conclude that the observed relationship between defect area and time to failure holds in general (under different test conditions or for different types

of bearings), so further test should be carried out and analyzed. Also, further work could focus on additional analyses of the statistical properties of defect regions. Additional characteristics that were estimated from the defect region analysis are the mean and standard deviation of the defect area clusters, the number of areas, and the single maximum defect area. These are currently not considered in the analysis, but potentially contain information to characterize the subsurface damage in even greater detail.

Conclusion

This paper analyses the accelerated WEC test method based upon FE8 type test rigs using axial cylindrical roller bearings. The main conclusions are:

- Load calculations show that the highest mechanical and frictional stress occurs at slightly different raceway positions and show a good correlation with the WEC affected area
- Time to failure analysis shows that WEC related failure can occur both prematurely and after surpassing the modified rated life time, with premature failures occurring at lower loads. Thus not all WEC related failure are to be considered premature and the load influence is lower than by classical RCF
- Using dynamic load did not accelerate WEC failure, even though peak stresses were higher. This indicates WEC failure mechanism in FE8 type test rigs is dependent on frictional loading ($p \cdot v_{sliding}$), where a constant load will have a higher energetic input than a dynamic load for a given running time
- Using dynamic loads caused only failure in the rollers. No presence of WEC was detected in the washers under dynamic loads using ultrasound scans, while extensive presence of WEC was found in the rollers
- The characterization of defect regions using advanced image analysis is a novel way to quantify subsurface damages in bearings. Constant load tests in TR1 & TR2 showed WEC failure could be achieved consistently, however there were seemingly large random variations in damage caused by tests run under the same conditions. These variations were quantified by the weighted area defect ratio. Although only based on a small sample, subsequent analysis showed that these variations correlate with failure times, indicating that image analysis is a powerful tool to quantify progressive bearing damage

Acknowledgements

This project was sponsored by the 2nd Joint Experiments of the IRPWIND project 2016 work program as well as by Innovation Fund Denmark grant number 7046-00003B. The tests in TR3 were conducted within the research project FVA 707 II (IGF-Nr. 17904) financed by the *AiF Arbeitsgemeinschaft industrieller Forschungsvereinigung "Otto von Guericke"e.V.*

References

[1] Evans MH: An updated review: white etching cracks (WECs) and axial cracks in wind turbine gearbox bearings, *Materials Science and Technology* **32** (2016) 1133-1169 DOI:10.1080/02670836.2015.1133022

[2] Stadler K, Lai J, Vegter RH: A Review: The Dilemma With Premature White Etching Crack (WEC) Bearing Failures, BEARING STEEL TECHNOLOGIES: 10TH VOLUME, ADVANCES IN STEEL TECHNOLOGIES FOR ROLLING BEARINGS, STP 1580, 2014

[3] Greco A, Sheng S, Keller J, Erdemir A: Material wear and fatigue in wind turbine Systems, *Wear* **302** (2013) 1583-1591 DOI:10.1016/j.wear.2013.01.060

[4] Al-Tameemi HA, Long H, Dwyer-Joyce RS: Initiation of sub-surface micro-cracks and white etching areas from debonding at non-metallic inclusions in wind turbine gearbox bearing, *Wear* **406–407** (2018) 22–32 DOI:10.1016/j.wear.2018.03.008

[5] Ganti S, Turner B, Kirsch M, Anthony D, McCoy B, Trivedi H, Sundar V: Three-dimensional (3D) analysis of white etching bands (WEBs) in AISI M50 bearing steel using automated serial sectioning, *Materials Characterization* **138** (2018) 11-18 DOI:10.1016/j.matchar.2018.01.010

[6] Grabulov A, Petrov R, Zandbergen HW: EBSD investigation of the crack initiation and TEM/FIB analyses of the microstructural changes around the cracks formed under Rolling Contact Fatigue (RCF), *International Journal of Fatigue* **32** (2010) 576–583 DOI:10.1016/j.ijfatigue.2009.07.002

[7] Garabedian NT, Gould BJ, Doll GL, Burris DL: The Cause of Premature Wind Turbine Bearing Failures: Overloading or Underloading?, *Tribology Transactions* (2018) DOI:10.1080/10402004.2018.1433345

[8] Dabrowski D, Natarajan A: Identification of loading conditions resulting in roller slippage in gearbox bearings of large wind turbines, *Wind Energy* **20** (2017) 1365–1387 DOI:10.1002/we.2098

[9] Errichello R, Budny R, Eckert R: Investigations of Bearing Failures Associated with White Etching Areas (WEAs) in Wind Turbine Gearboxes, *Tribology Transactions* **56** (2013) 1069-1076 DOI:10.1080/10402004.2013.823531

[10] Blass T, Dinkel M, Trojahn W: Bearing performance as a function of structure and heat treatment, *Materials Science and Technology* **32** (2016) 1079-1085 DOI:10.1080/02670836.2015.1120999

[11] Gould B, Paladugu M, Demas NG, Greco AC, Hyde RS: Figure the impact of steel microstructure and heat treatment on the formation of white etching cracks, *Tribology International* (2019) DOI:10.1016/j.triboint.2019.02.003.

[12] Evans RD, Hager CH, Logsdon: Friction and Wear Performance of Candidate Surface Treatments for Wind Turbine Gearbox Bearings in High Slip Contacts, Proceedings of the ASME/STLE 2009 International Joint Tribology Conference, IJTC2009, October 19-21, 2009, Memphis, Tennessee, USA

[13] Evans RD, Hager CH, Kang YS Doll GL: Comparison of Black Oxide and Tungsten Carbide–Reinforced Diamond-Like Carbon (WC=a-C:H) Surface Treatments for Rolling Element Bearings, *Tribology Transactions* **58** (2015) 444–453 DOI:10.1080/10402004.2014.983253

[14] Yamabe J, Takagoshi D, Matsunaga H, Yamada H, Uyama H: Hydrogen permeation of black oxide-treated and diamond-like carbon -coated bearing steels using high-pressure hydrogen gas, The 2017 world congress on Advances in structural engineering and mechanics (ASEM17), 28 August – 1 September 2017, Seoul, Korea

[15] Paladugu M, Lucas DR, Hyde RS: Effect of lubricants on bearing damage in rolling-sliding conditions: Evolution of white etching cracks, *Wear* **398–399** (2018) 165–177 DOI:10.1016/j.wear.2017.12.001

[16] Haque T, Korres S, Carey JT, Jacobs PW, Loos J, Franke J: Lubricant Effects on White Etching Cracking Failures in Thrust Bearing Rig Tests, *Tribology Transactions* (2018) DOI:10.1080/10402004.2018.1453571

[17] Ruellan A, Ville F, Kleber X, Arnaudon A, Girodin D: Understanding white etching cracks in rolling element bearings: The effect of hydrogen charging on the formation mechanisms, *Proc IMechE Part J: J Engineering Tribology* **228** (2014) 1252–1265 DOI:10.1177/1350650114522452

[18] Gould B, Demas NG, Pollard G, Rydel JJ, Ingram M, Greco AC: The Effect of Lubricant Composition on White Etching Crack Failures, *Tribology letters* **67** (2019) DOI:10.1007/s11249-018-1106-y

[19] Evans MH, Richardson AD, Wang L, Wood RJK: White etching crack (WEC) investigation by serial sectioning, focused ion beam and 3-D crack modelling, *Tribology International* **65** (2013) 146-160 DOI:10.1016/j.triboint.2013.03.022

[20] Mikami H, Kawamura T: Influence of Electrical Current on Bearing Flaking Life, SAE Technical Paper 2007-01-0113, SAE International: Warrendale, PA.

[21] Loos J, Bergmann I, Goss M: Influence of Currents from Electrostatic Charges on WEC Formation in Rolling Bearings, *Tribology Transactions* **59** (2016) 865–875 DOI:10.1080/10402004.2015.1118582

[22] Evans MH, Richardson AD, Wang L, Wood RJK, Anderson WB: Confirming subsurface initiation at non-metallic inclusions as one mechanism for white etching crack (WEC) formation, *Tribology International* **75** (2014) 87-97 DOI:10.1016/j.triboint.2014.03.012

[23] Holweger W, Wolf M, Merk D, Blass T, Goss M, Loos J, Barteldes S, Jakovics A: White Etching Crack Root Cause Investigations, *Tribology Transactions* **58** (2015) 59-69 DOI:10.1080/10402004.2014.942938

[24] Diederichs AM, Barteldes S, Schwedt A, Mayer J, Holweger W: Study of subsurface initiation mechanism for white etching crack formation, *Materials Science and Technology* **32** (2016) 1170-1178 DOI:10.1080/02670836.2016.1155842

[25] Danielsen HK, Gutiérrez Guzmán F, Dahl KV, Li YJ, Wu J, Jacobs G, Burghardt G, Fæster S, Alimadadi H, Goto S, Raabe D, Petrov R: Multiscale characterization of White Etching Cracks (WEC) in a 100Cr6 bearing from a thrust bearing test rig, *Wear* **370–371** (2017) 73-82 DOI:10.1016/j.wear.2016.11.016

[26] Gutiérrez Guzmán F, Oezel M, Jacobs G, Burghardt G, Broeckmann C, Janitzky T: Reproduction of white etching cracks under rolling contact loading on thrust bearing and two-disc test rigs, *Wear* **390–391** (2017) 23-32 DOI:10.1016/j.wear.2017.06.020

[27] Richardson AD, Evans MH, Wang L, Wood RJK, Ingram M, Meuth B: The Evolution of White Etching Cracks (WECs) in Rolling Contact Fatigue-Tested 100Cr6 Steel, *Tribology Letters* **66** (2018) DOI:10.1007/s11249-017-0946-1

[28] Franke J, Carey JT, Korres S, Haque T, Jacobs PW, Loos J, Kruhoeffer W: White Etching Cracking—Simulation in Bearing Rig and Bench Tests, *Tribology Transactions* **61** (2018) 403-413 DOI:10.1080/10402004.2017.1339839

[29] Kruhöffer W, Loos J: WEC Formation in Rolling Bearings under Mixed Friction: Influences and "Friction Energy Accumulation" as Indicator, *Tribology Transactions* **60** (2017) 516-529 DOI:10.1080/10402004.2016.1183250

[30] DIN 51819-1:2016-12, Testing of lubricants - Mechanical-dynamic testing in the roller bearing test apparatus FE8 - Part 1: General working principles

[31] DIN 51819: Testing of lubricants—Mechanical-dynamic testing in the roller bearing test apparatus FE8. Edition December 1999.

[32] ISO 281:2007, Rolling bearings - Dynamic load ratings and rating life

[33] D. Dowson, G.R. Higginson: Elasto-Hydrodynamic Lubrication, Pergamon Press, Oxford, 1977

[34] Polonsky IA, Keer LM: A numerical method for solving rough contact problems based on the multi-level multi-summation and conjugate gradient techniques, *Wear* **231** (1999) 206–219 DOI:10.1016/S0043-1648(99)00113-1

[35] Gallego, L.; Nélias, D.; Deyber, S. (2010): A fast and efficient contact algorithm for fretting problems applied to fretting modes I, II and III. In Wear 268 (1-2), pp. 208–222. DOI: 10.1016/j.wear.2009.07.019.

[36] Liu S, Wang Q: Studying Contact Stress Fields Caused by Surface Tractions With a Discrete Convolution and Fast Fourier Transform Algorithm, *Journal of Tribology* **124** (2001) 36-45 DOI:10.1115/1.1401017

[37] Gupta PK: Advanced Dynamics of Rolling Element, Springer Verlag (1984)

[38] Pape F, Muhmann C, Pahl D, Lipinsky D, Arlinghaus HF, Poll G: ZDDP Containing Tribofilms Generated under Sliding Micro Contact and Bearing Test Rig Conditions, Materials Performance and Characterization 7, no. 3 (2018): 191-212. https://doi.org/10.1520/MPC20170067

[39] Gutierrez Guzman F, Oezel M, Pinar P: Risse auf Lagerringen II, FVA 707 II, Heft Nr. 1229, Forschungsvereinigung Antriebstechnik e.V., Frankfurt, 2017

[40] Danielsen HK, Carrasco AJ, Fæster S, Dahl KV, Gutierrez Guzman F, Sauvage P, Jacobs G: 3D X-ray computerized tomography of White Etching Cracks (WEC), *Materials Characterization* **150** (2019) 78-87 DOI:10.1016/j.matchar.2019.01.032

[41] DIN EN 61649:2008, Weibull-Analyse (IEC 61649 (2008-08))

[42] Bertsche B: Zuverlässigkeit im Fahrzeug- und Maschinenbau, VDI-Buch. Springer (2004), Berlin. DOI:10.1007/3-540-34996-0

[43] Vlcek BL, Hendricks C, Zaretsky EV: Monte Carlo Simulation of Sudden Death Bearing Testing, *Tribology Transactions* **47** (2004) 188-199, DOI:10.1080/05698190490431867

[44] Stadler K: White Etching Cracks - A symptom of bearing failures, FVA Bearing World (2016)

[45] Abernethy RB: The new Weibull handbook: Reliability & statistical analysis for predicting life, safety, risk, support costs, failures, and forecasting warranty claims. 5. Aufl. North Palm Beach (FL): R.B. Abernethy, (2006). ISBN 9780965306232

[46] Evans MH: An updated review: white etching cracks (WECs) and axial cracks in wind turbine gearbox bearings, *Materials Science and Technology* **32** (2016) 1133-1169 DOI:10.1080/02670836.2015.1133022

[47] Stadler K: White Etching Cracks - A symptom of bearing failures, FVA Bearing World (2016)

[48] Loos J, Blass T, Franke J, Kruhöffer W, Bergmann I: Influences on Generation of White Etching Crack Networks in Rolling Bearings, *Journal of Mechanics Engineering and Automation* **6** (2016) 85-94 DOI:10.17265/2159-5275/2016.02.004

[49] Genschel U, Meeker WQ: A Comparison of Maximum Likelihood and Median-Rank Regression for Weibull Estimation, Quality Engineering (2010), 22:4, 236-255, DOI: 10.1080/08982112.2010.503447

[50] Paladugu M, Hyde RS: Microstructure deformation and white etching matter formation along cracks, *Wear* **390-391** (2017) 367 – 375 DOI:10.1016/j.wear.2017.08.014

[51] Otsu N: A threshold selection method from gray-level histograms, *IEEE Transaction on Systems, Man, and Cybernetics* **9** (1979) 62-66 DOI:10.1109/TSMC.1979.4310076

[52] Meyer F: Topographic distance and watershed lines, *Signal Processing* **38** (1994) 113-125 DOI:10.1016/0165-1684(94)90060-4

Appendix A:

The bearing life calculations based in the work of Lundberg/Palmgren and Ioannides/Harris are standardized in DIN ISO 281 [32]. The calculations permit the determination of the number of load cycles a roller bearing will last under a known load and speed within a specific confidence level (usually 90 %). The so-called modified rated life time L_{mn} used in this work is defined as:

Equation 2: $$L_{nm} = a_1 \cdot a_{ISO} \cdot \left(\frac{C}{P}\right)^p = a_1 \cdot a_{ISO} \cdot L_{10} \; with \; a_{ISO} = f\left(\kappa, e_c, \frac{C_u}{P}\right)$$

The confidence level is determined by the factor a_1, which is 1 for a 90 % confidence level. The introduction of the life factor a_{ISO} (Eq. 2) allows, in contrast to the rated life time L_{10} (Eq. 2), the consideration of system parameters such as lubricating conditions and lubricant contamination. Here, the viscosity ratio κ, the impurity factor e_c, the fatigue limit load C_u and the equivalent load P are taken into account. A further description of the single parameters as well as guideline values are defined in the current version of DIN ISO 281 [48]. The values used in this work are:

Life exponent (roller bearings)	p	10/3
Dynamic load rating	C	137 – 172 kN
Bearing thrust load	P	60 – 80 kN
Speed of rotation	n	300 rpm
Viscosity ratio	κ	0.24
Contamination factor	e_c	1
Fatigue load limit	C_u	35-47.5 kN

Herewith the life factor a_1 is determined in this work as follows (Eq. 3):

Equation 3 $$a_{ISO} = 0.1 * \left[1 - \left(1.5859 - \frac{1.3993}{0.24^{0.054381}}\right) * \left(\frac{C_u}{2.5 * P}\right)^{0.4}\right]^{-9.185}$$